

Chapter 3

Geologic Applications of Roughness Maps

Parts of the work presented here were originally prepared for and published in:

Zuber, M. T., J. W. Head, D. E. Smith, G. A. Neumann, E. Mazarico, M. H. Torrence, O. Aharonson, A. R. Tye, C. I. Fassett, M. A. Rosenburg, et al. (2012a), Constraints on the volatile distribution within Shackleton crater at the lunar south pole, *Nature*, 486(7403), 378–381

and

Kreslavsky, M. A., J. W. Head, G. A. Neumann, M. A. Rosenburg, O. Aharonson, D. E. Smith, and M. T. Zuber (2013), Lunar topographic roughness maps from Lunar Orbiter Laser Altimeter (LOLA) data: Scale dependence and correlation with geologic features and units, *Icarus*, 226(1), 52–66

3.1 Introduction

Surface roughness maps are valuable tools for geologic mapping and interpretation because they provide a means of analyzing large-scale variations in the typical character of textures at smaller scales. Identification of these variations can aid in defining geologic units, determining their relative ages, and characterizing the dominant surface processes acting at different scales to produce and modify topography. Moreover, roughness calculations derived from spacecraft observations, like those computed with topography data from the Lunar Orbiter Laser Altimeter (LOLA) carried on the Lunar Reconnaissance Orbiter (LRO) (*Smith et al.*, 2010a), rely on differences between successive elevation measurements, thus exploiting the exceptional precision in ranging along each orbit, which is much higher than the precision in overall orbit determination (*Smith et al.*, 2010b; *Kreslavsky et al.*, 2013). By utilizing this high internal precision, roughness calculations therefore maximize the differential topographic information returned.

As discussed in the previous chapter, roughness can be defined in many different ways, and several roughness parameters are typically employed for different purposes. This profusion of definitions led *Kreslavsky et al.* (2013) to describe six key qualities that roughness parameters must be assessed on for use in geological interpretation: 1) intuitive character; 2) independence with respect to regional tilts; 3) ability to capture typical surface textures; 4) specificity of scale; 5) statistical stability; and 6) tolerance of individual peculiarities within the dataset used (*Kreslavsky et al.*, 2013). These requirements are often in conflict, and no roughness parameter is ideal in all aspects. For example, the RMS slope (defined in Eq. 2.1) is often reported because it can be related to measurements of radar reflection scatter, and it is also an intuitive measure of surface roughness, satisfying requirement (1). However, because the RMS slope is sensitive to even a small proportion of steep slopes, and because topographic surfaces tend to have slope-frequency distributions with heavy tails, this parameter fails criteria (3) and (5).

For purposes of discrimination among geologic units, the median differential slope described in the previous chapter and *Rosenburg et al.* (2011) satisfies many of the key criteria and possesses several useful characteristics. Defined in Equation 2.3, the differential slope isolates features on a given scale of interest, L , by subtracting the slope at twice this scale, $2L$. It is thus unaffected by larger-scale, regional tilts (criterion 2) and describes a well-defined, specific scale (criterion 4), allowing for detailed examination of scale dependence in surface roughness. Reporting the median differential slope within each sliding window along a LOLA track guarantees that the roughness values reported are typical of the region and not overly influenced by a few unusually high values (criterion 3). While this parameter satisfies these criteria, there is a tradeoff with criterion (1). Because the reported values are slopes at a given scale measured with respect to slopes at twice that scale, differential slope is not as intuitive a measure of surface roughness as the RMS slope or RMS height. Nevertheless, it is useful for emphasizing roughness variations and distinguishing among geologic units.

Rosenburg et al. (2011) (see also Chapter 2) presented the first global roughness maps utilizing topography data from LOLA, introducing a variety of roughness parameters, including median slope,

bidirectional slope, differential slope, and Hurst exponent (Chapter 2). *Kreslavsky et al.* (2013) extended this global analysis, using a related roughness parameter, the topographic curvature, at hectometer and kilometer scales. These studies investigate the scale dependence of surface slopes and provide a global context for regional roughness variations, to which more detailed surveys of local roughness can be referenced. This chapter focuses on two such investigations, using the full range of data collected during LRO’s nominal and science mission phases. First, the lunar south pole is examined in detail, with particular attention to Shackleton crater and the progression of roughness signatures among craters and basins of increasing size, from simple craters to ringed basins. Second, the analysis of roughness on mare surfaces in Chapter 2 is extended to examine the relationship between scale-dependent roughness and surface age.

3.2 Lunar South Pole

During the mapping and science phases of the mission, which extended from September, 2010, through December, 2013, LRO traveled in a consistent 50-km polar orbit, a geometry that resulted in a confluence of tracks over the north and south poles. The high density of measurements available in these regions allows for a much greater resolution in gridded data (*Zuber et al.*, 2012a), as well as a higher density of along-track roughness calculations than is globally available. Figure 3.1 contains a color composite map of the median differential slope extending from 60°S to the south pole, showing roughness at three different scales, consistent with the global maps shown above in Figure 2.5. The smallest scale for slope calculations accessible to LOLA is equivalent to the shot spacing, approximately 57 m. Slopes at this scale and twice this scale (~ 110 m) were computed and binned in $1/64^\circ$ (~ 480 m) overlapping windows along each orbit track, and the windows were spaced $1/128^\circ$ (~ 240 m) apart. After aligning the resulting slope profiles, the values were subtracted and the median differential slope for each window was reported at the midpoint. This process was repeated for slopes at many other scales, three of which were combined to produce the composite image shown in Figure 3.1. Small-scale slopes (~ 57 m) are shown in the blue channel, intermediate scales (~ 220 m) in green, and larger scales (~ 560 m) in red. The pixel resolution is $1/64^\circ$, or

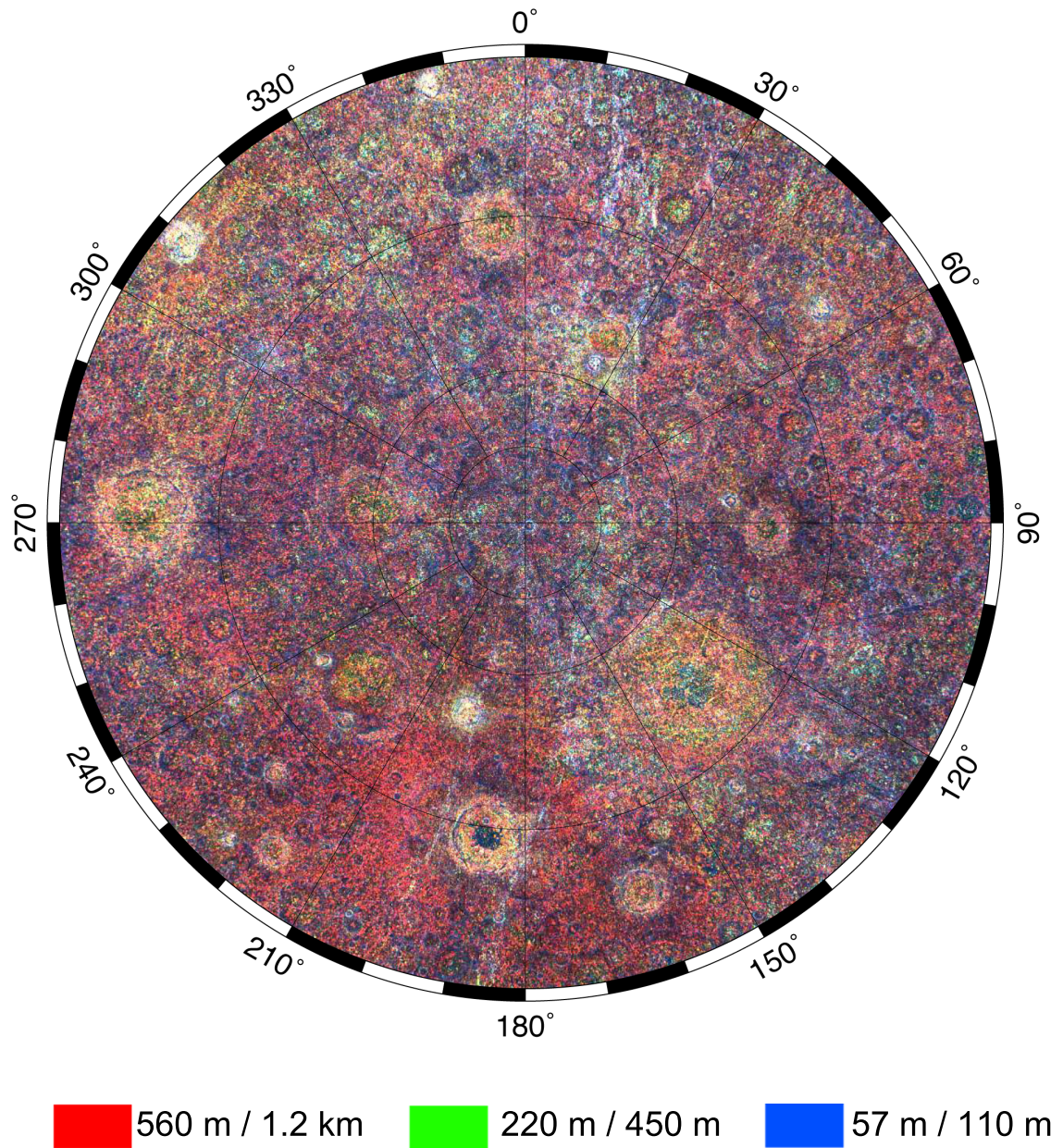


Figure 3.1: Median differential slope map of the lunar south pole from 60°S, showing differential slopes at three scales in the three color channels as in Figure 2.5. The blue channel corresponds to differential slopes at ~ 57 m, green corresponds to ~ 220 m, and red ~ 560 m.

approximately 0.48 km.

This map represents a significant improvement in resolution compared to Figure 2.5, made possible in part by the inclusion of more LOLA tracks, but also by the confluence of tracks over the poles due to orbit geometry. Several observations made in the previous chapter on global roughness are also apparent here. For example, the brightest features are young, Copernican-age craters which appear white in the composite image because they are rough at every scale included. Prominent features include the craters De Forest (77.3°S, 162.1°W), Zucchius (64.1°S, 50.3°W), and Rutherford (60.9°S, 12.1°W), all of which have associated ray systems that appear as star-shaped enhancements in intermediate scales (green shades) outside the crater rims. Several very long, bright, linear features are also visible extending from lower latitudes and crossing near the pole. One pair of these features is associated with the crater Tycho (43.3°S, 11.4°W), which is thought to be the youngest feature of its size on the lunar surface (*Kreslavsky et al.*, 2013). The rays are not always associated with distinct topographical relief, but nevertheless contain a unique signature in the differential slope map. They deviate very little from great circles and are brightest on the near side, closest to Tycho. As noted by *Kreslavsky et al.* (2013), these rays are composed of regions of relatively smoother and rougher segments, the latter corresponding to clusters of secondary craters.

3.2.1 Large Craters and Basins

Aside from the bright young craters and the long linear rays, the most noticeable features in Figure 3.1 are the large craters and basins that range in size from ~ 50 to ~ 300 km in the case of Schrödinger (75°S, 134.4°E). At the scales included in this differential slope map, craters in this range of diameters are characterized by a distinctive set of features which follow the progression of crater morphology from large complex craters with central peaks to multi-ring basins. Lyman (64.8°S, 163.6°E) is a $D = 84$ km crater that has undergone relatively little erosion by subsequent impacts. Figure 3.2 shows a portion of the Lunar Reconnaissance Orbiter Camera (LROC) Wide Angle Camera (WAC) Mosaic centered on the crater, with an inset showing the corresponding portion of the differential slope map shown in Figure 3.1. The roughly circular rim crest is visible as

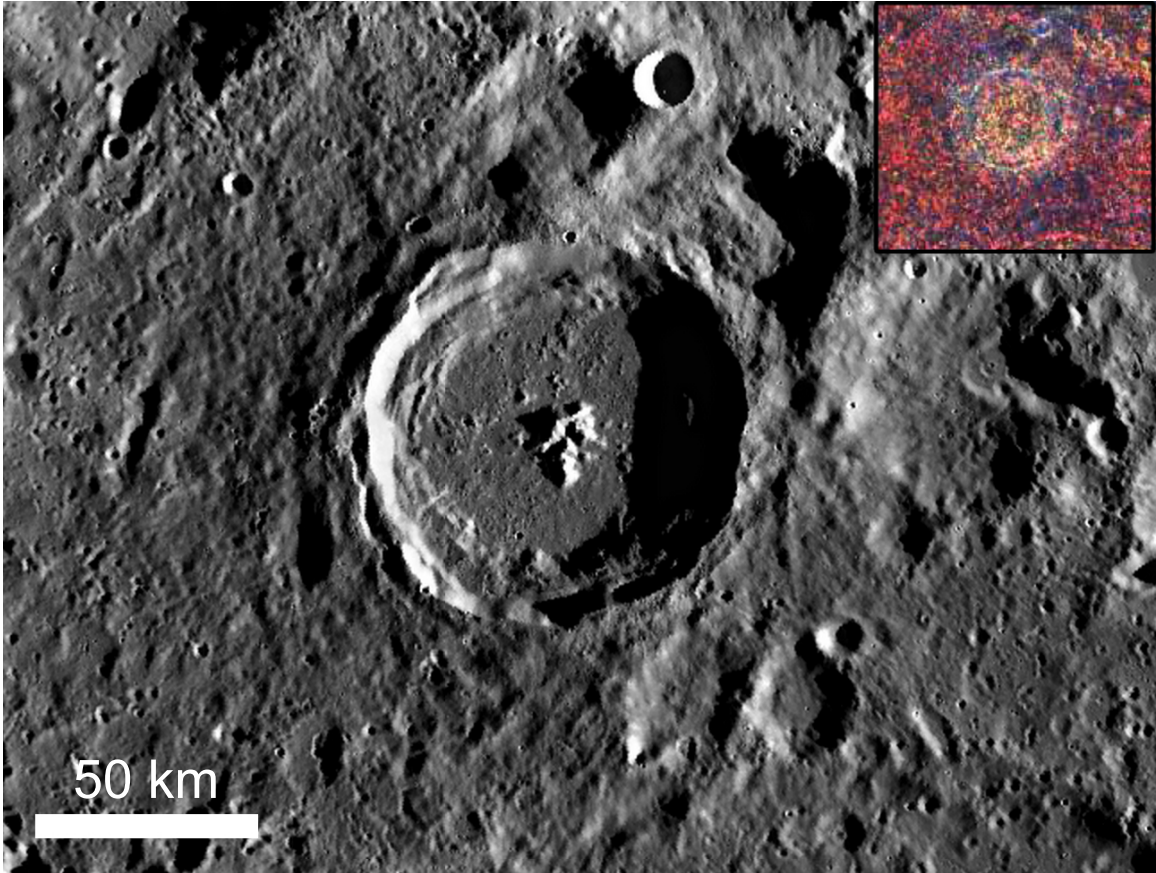


Figure 3.2: Lyman crater (74.2°S , 90.8°E) shown in the LROC WAC mosaic in a south polar stereographic projection. The inset shows the corresponding portion of the median differential slope map shown in Figure 3.1.

a bright white ring that is largely uninterrupted around the crater perimeter, indicating that the sharp relief at the rim crest is registered in slopes at the scales represented by all channels. Just inside the rim, a dark blue ring defines the steep inner walls, which are quite smooth at all scales; only the smallest scale (~ 57 m) shows any signal at all, consistent with the effects of mass wasting observed both within and without the crater rim. The slumped material forms a ring on the crater floor that appears with a red hue in the differential slope map, reflecting its hummocky character on kilometer scales. The prominent central peak formation appears with a similar hue, while the remainder of the crater floor is roughest at intermediate scales, resulting in a somewhat yellower appearance mottled with darker regions of relatively smooth terrain.

This bullseye pattern of concentric rings corresponding to the morphologic features is found in many other complex craters shown in Figure 3.1 with some important variations. For example, Hale

(74.2°S, 90.8°E) is a relatively young impact crater of nearly the same size as Lyman ($D = 83$ km), containing few superposed craters, but its multiply terraced rim is expressed as a wide annulus of enhanced roughness at the largest scale (~ 560 m), rather than a continuous bright ring. The floor of Hale is also somewhat smoother than that of Lyman, appearing as a dark blue ring surrounding the central peak complex, which is offset from the center toward the south. The slightly larger crater Demonax ($D = 114$ km, 78.2°S, 59.0°E) is much more heavily eroded, and its smoother walls form a wide dark annulus around the bright crater floor, which is relatively level and contains both hummocky, mass-wasted material (red, roughest at the 560-m scale) and flat terrain punctuated by kilometer-scale craters (yellow, roughest at the 220-m scale). These variations in roughness signature among complex craters of similar size thus provide useful markers for identifying crater age and degree of degradation. This is an important feature, especially at the lunar poles, where illumination conditions are highly variable and regions of permanent shadow persist in the floors of many circumpolar craters. Gridded digital elevation models from LOLA can be used to count craters in these regions, but roughness analysis like that presented here provides another means of assessing relative ages.

Antoniadi (69.7°S, 172.0°W) is a large peak ring crater ($D = 143$ km)—one of only a few features possessing both a central peak and a surrounding inner ring (*Wilhelms et al.*, 1987), a transitional morphology between complex craters and ringed basins that is not well understood. Located within the South Pole-Aitken Basin, Antoniadi also happens to contain the lowest elevation on the Moon (*Smith et al.*, 2010b). Like its smaller counterparts, this crater has a sharp rim crest defined by a bright white ring, although in this case the ring is not continuous. The steep inner walls form a dark blue ring, part of which corresponds to the brightly illuminated north wall in the LROC WAC Mosaic shown in Figure 3.3. The region between the walls and the inner ring is rough at the ~ 220 -m scale, while the chain of mountain segments making up the ring itself is distinguishable as a somewhat redder annulus, reflecting the change in texture. Likewise, the central peak and other isolated massifs visible inside the inner ring are rough only at the largest scale, ~ 560 m.

The interior of the inner ring is covered with a young mare deposit (*Wilhelms et al.*, 1979),

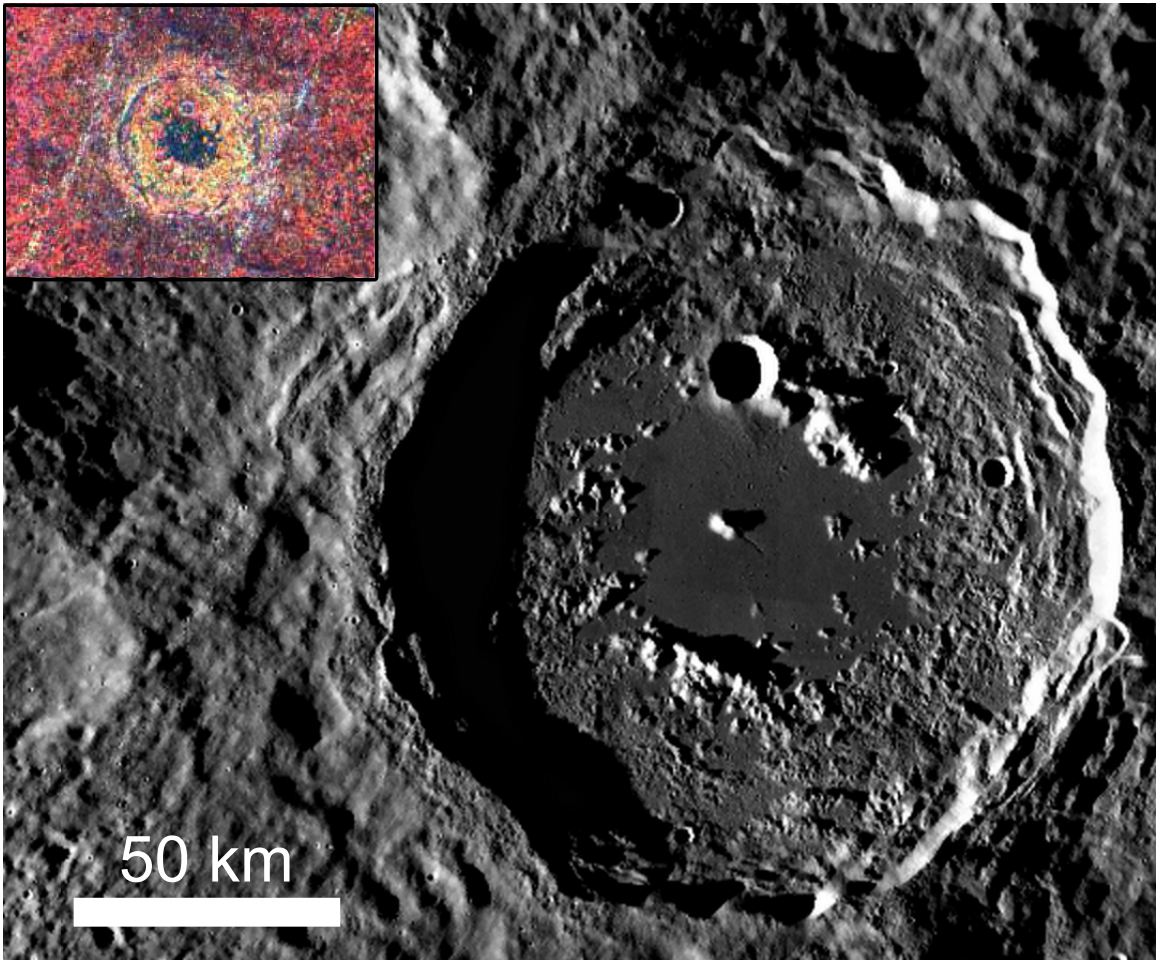


Figure 3.3: Antoniadi crater (69.7°S , 172.0°W) shown in the LROC WAC mosaic in a south polar stereographic projection. The inset shows the corresponding portion of the median differential slope map shown in Figure 3.1.

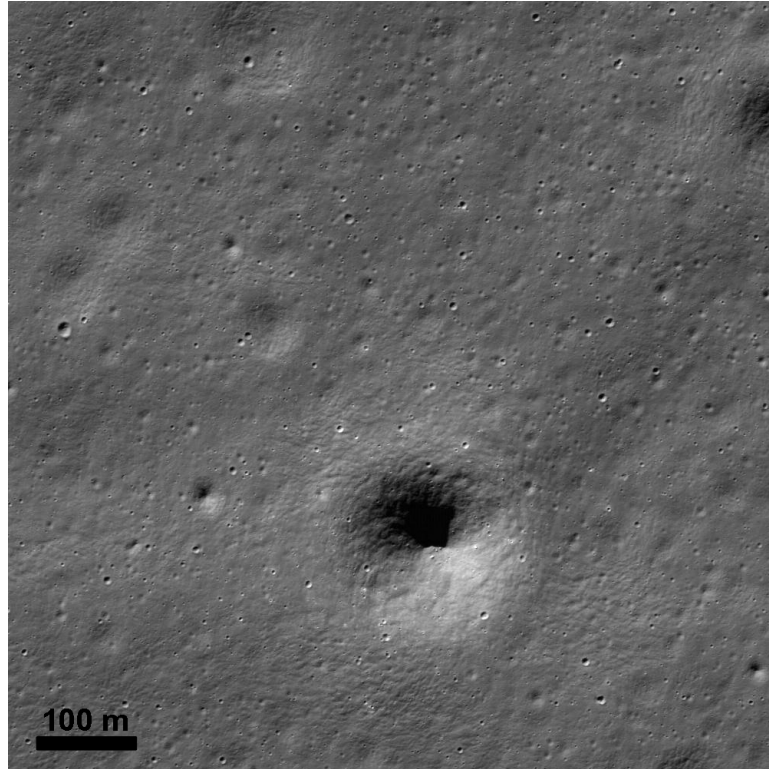


Figure 3.4: Mare deposits on the floor of Antoniadi, shown in a portion of LROC NAC image M1130635802R.

and its roughness signature is similar to those of comparably young mare-filled basins on the near side of the moon shown in Figure 2.5. This unit is relatively smooth at all scales shown in the composite image, with most signal present in the smallest LOLA scale, ~ 57 m. Figure 3.4 shows the floor of Antoniadi within the inner ring from a portion of the LROC Narrow Angle Camera (NAC) image M1130635802R. The mare surface is covered with small craters down to sizes below the image resolution (~ 1 m/pix). Some craters appear relatively pristine, but many others, like the largest feature shown ($D \sim 180$ m), have been smoothed by the diffusive action of regolith gardening (see Chapter 4). Craters like this one contribute to the differential slope at the ~ 57 -m scale, but appear smooth at larger scales, as shown in Figure 3.3.

Aside from the South Pole-Aitken Basin, Schrödinger (75.0°S , 132.4°E) is the largest basin poleward of 60°S (Figure 3.1), with $D = 312$ km. The basin and the corresponding section of the differential slope map are shown in Figure 3.5. As with Antoniadi and Lyman, distinct roughness zones can be identified that correspond to morphologic features of the basin. Schrödinger's rim is a

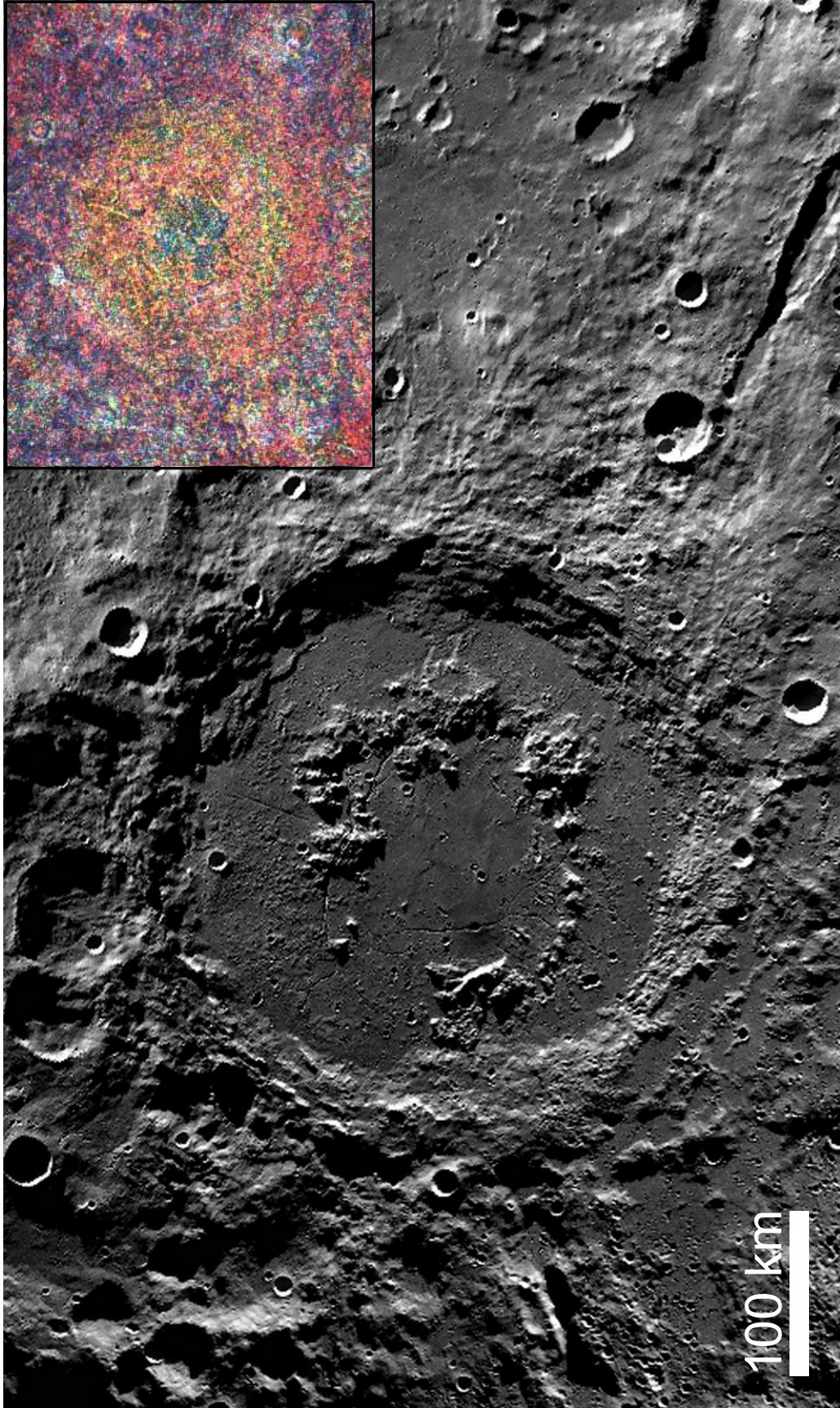


Figure 3.5: Schrödinger basin (75.0°S , 132.4°E) shown in the LROC WAC mosaic in a south polar stereographic projection. The inset shows the corresponding portion of the median differential slope map shown in Figure 3.1.

broad, terraced annulus that is roughest at the largest scale included in the composite image, ~ 560 m. The inner ring, which occurs at about half the crater diameter, has a similar hue, reflecting the kilometer-scale roughness of the rugged chain of mountain segments. Between the walls and the inner ring, the floor is relatively bright and roughest at intermediate scales (~ 220 m), appearing yellow. Within the inner ring, where the surface has been reworked by lava flows and impact gardening, the shortest scale dominates and the area appears blue in the composite map, much brighter (rougier) than Antoniadi's mare-filled interior. Several distinctive tectonic features are easily seen in the roughness map, including many of the radial and concentric fractures that traverse the crater floor, sometimes crossing the peak ring (*Mest*, 2011).

Several smaller craters ($D < 50$ km) with characteristic roughness signatures are visible in Figure 3.5 outside the rim of Schrödinger. The rough rim crest appears as a bright white ring, within which the steep crater walls appear dark blue. The center of each crater is distinctively rough at larger scales (~ 220 – 560 m), appearing orange in the color composite image. This particular pattern of concentric roughness zones characterizes many craters in this size range throughout Figure 3.1, including Shackleton crater, a feature of great interest because of its location so near to the south pole and, consequently, the unique illumination conditions.

3.2.2 Shackleton Crater

Shackleton crater, nearly centered at the lunar south pole (89.9°S , 0°E), is a relatively fresh 21-km crater. The floor is almost entirely in permanent shadow, while the walls receive continuous sunlight, due to the Moon's low inclination, and, as a result, the floor of the crater is a perennial cold trap (*Watson et al.*, 1961; *Arnold*, 1979). However, whether lunar volatiles are present within the crater or other permanently shadowed regions (PSRs) remains an open question, as previous orbital and Earth-based radar mapping and imaging missions have returned conflicting results (*Nozette et al.*, 1996; *Stacy et al.*, 1997; *Campbell et al.*, 2006; *Simpson and Tyler*, 1999; *Nozette et al.*, 2001). LOLA illuminates the surface at a wavelength of 1064 nm, allowing for brightness measurements of PSRs at that wavelength in the absence of sunlight. *Zuber et al.* (2012a) found that the walls of Shackleton

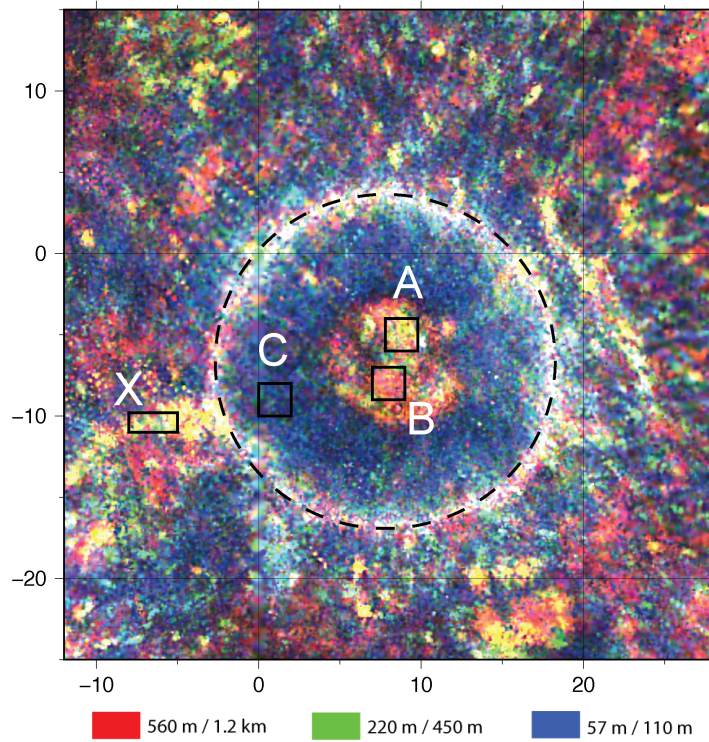


Figure 3.6: Color composite image showing differential slope at three scales: 560 m (10 LOLA shot spacings) in the red channel, 220 m (4 shot spacings) in green, and 57 m (1 shot spacing) in blue. The median differential slope at each scale is reported for overlapping windows of width $1/64^\circ$ (~ 480 m), spaced $1/128^\circ$ (~ 240 m) apart. Boxes represent regions sampled to create Figure 3.7, and the location of the rim crest is shown as a dashed black line. Several distinct roughness units are apparent within Shackleton Crater. The crater walls, which are smooth at large scales, retain roughness only at the smallest scales, causing them to appear dark blue. The crater floor, which contains a hummocky mound unit that is smooth at all scales but roughest at large scales, thus appearing red in the image, and a flat region, which is roughest at intermediate and large scales, thus appearing yellow. Outside the rim, secondary crater fields identified in *Zuber et al.* (2012a) (Figure 1e) appear as yellow streaks due to their unique contribution to the topography at intermediate and large scales.

crater are anomalously bright, and the crater floor, while darker than the walls, is brighter than the surrounding terrain. These observations are consistent with downslope movement of regolith, exposing fresher material in the crater walls, and decreased space weathering on the crater floor due to shadowing. The brightness of the floor at 1064 nm could also be explained by a 1-mm-thick layer of regolith containing $\sim 20\%$ water ice (Zuber *et al.*, 2012a).

A detailed examination of surface roughness in the vicinity of Shackleton crater reveals several distinct roughness units. Figure 3.6 is a color composite image showing the median differential slope at three baselines, as in Figure 3.1: ~ 57 meters in the blue channel, ~ 220 meters in green, and ~ 560 meters in red. The boxes mark sampled regions within each roughness unit, and differential slopes are shown in Figure 3.7 for a variety of scales. The walls of the crater (Fig. 3.6, C) are smooth at the large and intermediate scale, retaining roughness only at the shortest scale and thus appearing blue in the image. The floor can be divided into two regions, a flat portion (Fig. 3.6, A) and an elevated terrain possibly related to mass wasting at the crater walls (Fig. 3.6, B). The roughness of this mound unit increases at the largest scales due to its hummocky character, but it is smoother than the flat region at all scales < 850 m, due to its paucity of craters. In fact, at the shortest scales the mound is the smoothest of the representative regions shown. The flat floor has a higher crater age and appears yellow due to the addition of slopes on the intermediate scale, while the rim itself, the crest of which is marked by a dashed black line in Figure 3.6, is rough at all scales, appearing white. Areas of suspected secondaries (Fig. 3.6, X) are clearly defined in the roughness map as yellow streaks, owing to high slopes at the largest and intermediate scales and little roughness at the smallest scale. The distinct character of these roughness units and their correlation with mapped geologic units using gridded topography data illustrates the usefulness of roughness maps for clarifying relationships between superposed units. For example, secondary craters are often difficult to distinguish from primary craters of similar diameters in visual imagery. However, because they are often formed at lower velocities than primary craters, they tend to have different morphologies and depth-to-diameter scaling relationships. As Figure 3.6 shows, they contribute a unique signature to the topographic roughness that can aid in their identification and mapping.

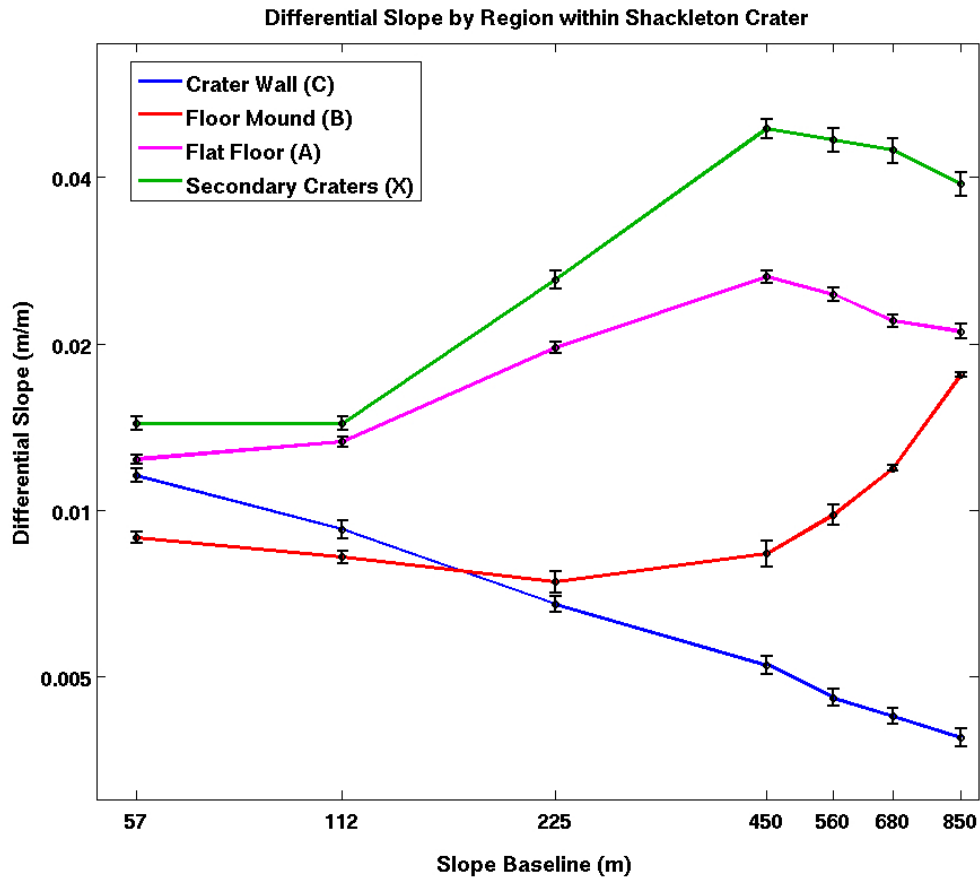


Figure 3.7: Differential slope for several baselines corresponding to 1, 2, 4, 8, 10, 12, and 15 LOLA shot spacings, showing roughness variation with scale for several distinct roughness units related to Shackleton crater. The region sampled for each roughness unit is marked by a box in Figure 3.6. Labels correspond to the regions mapped for crater counting in *Zuber et al. (2012a)* (Figure 1e). The crater wall (Fig. 3.6, C) is smooth at large scales and retains roughness only at the smallest scale, while the hummocky terrain on the crater floor (Fig. 3.6, B) is smooth at small and intermediate scales, becoming rougher at large scales. The flat part of the crater floor (Fig. 3.6, A) is roughest at intermediate scales, similar to the clusters of suspected secondary craters (Fig. 3.6, X). Standard 2σ error bars represent the spread of the distribution of median differential slopes within each sampled region and for each baseline considered.

3.3 Roughness of Mare Surfaces

As discussed above, the median differential slope is a powerful tool for discriminating between roughness units. It can also help us to understand the evolution of roughness on surfaces of varying age, particularly in the lunar maria. *Farr* (1992) explored the development of surface roughness at centimeter- to meter-scales on progressively older terrestrial lava flows, showing that particular features in the topographic power spectrum could be correlated with specific geologic processes occurring on these surfaces, such as aeolian deposition and fluvial dissection. On the Moon, the major roughening agent at every scale is the accumulation of impact craters. The power law exponent of the observed cumulative size-frequency distributions in the maria is negative for sub-kilometer craters, at approximately -4 (*Melosh*, 1989; *Neukum et al.*, 2001), indicating that small craters are much more numerous than large ones. Thus, resurfaced areas collect small craters first and accumulate successively larger ones over time. Roughness on surfaces of varying age is expected to reflect this sequence, the younger surfaces remaining smoother at larger scales. Older surfaces, which have had time to collect craters over a greater range of diameters, are expected to have significant roughness components at intermediate and larger scales.

In Figures 2.5 and 3.1, mare deposits generally appear dark blue because they are relatively smooth, and what roughness does exist occurs at the smallest scale studied (~ 57 m), which is shown in the blue channel of the composite images. However, variations in hue are apparent between different mare regions. Comparing the differential slope at many different scales ranging from ~ 57 m to ~ 1.4 km, we find a trend that corresponds to the reported ages of various mare units, as estimated by *Hiesinger et al.* (2010) from detailed crater counts. Figure 3.8 contains a context map in which the outline of the mare deposits (*Wilhelms et al.*, 1971, 1977; *Scott and McCauley*, 1977; *Lucchitta and Center*, 1978; *Stuart-Alexander and Center*, 1978; *Wilhelms et al.*, 1979) are overlain on the elevation map, and sampled regions are marked by lettered boxes. Figure 3.9 shows the differential slope at several baselines for the regions sampled, which range from the oldest dated flows in Mare Marginis and Mare Tranquilitatis (> 3.6 Ga) to flows of intermediate age in Mare Humorum (~ 3.3 Ga) and Mare Imbrium (~ 2.7 Ga), to the youngest dated unit in Oceanus Procellarum (< 2.5 Ga)

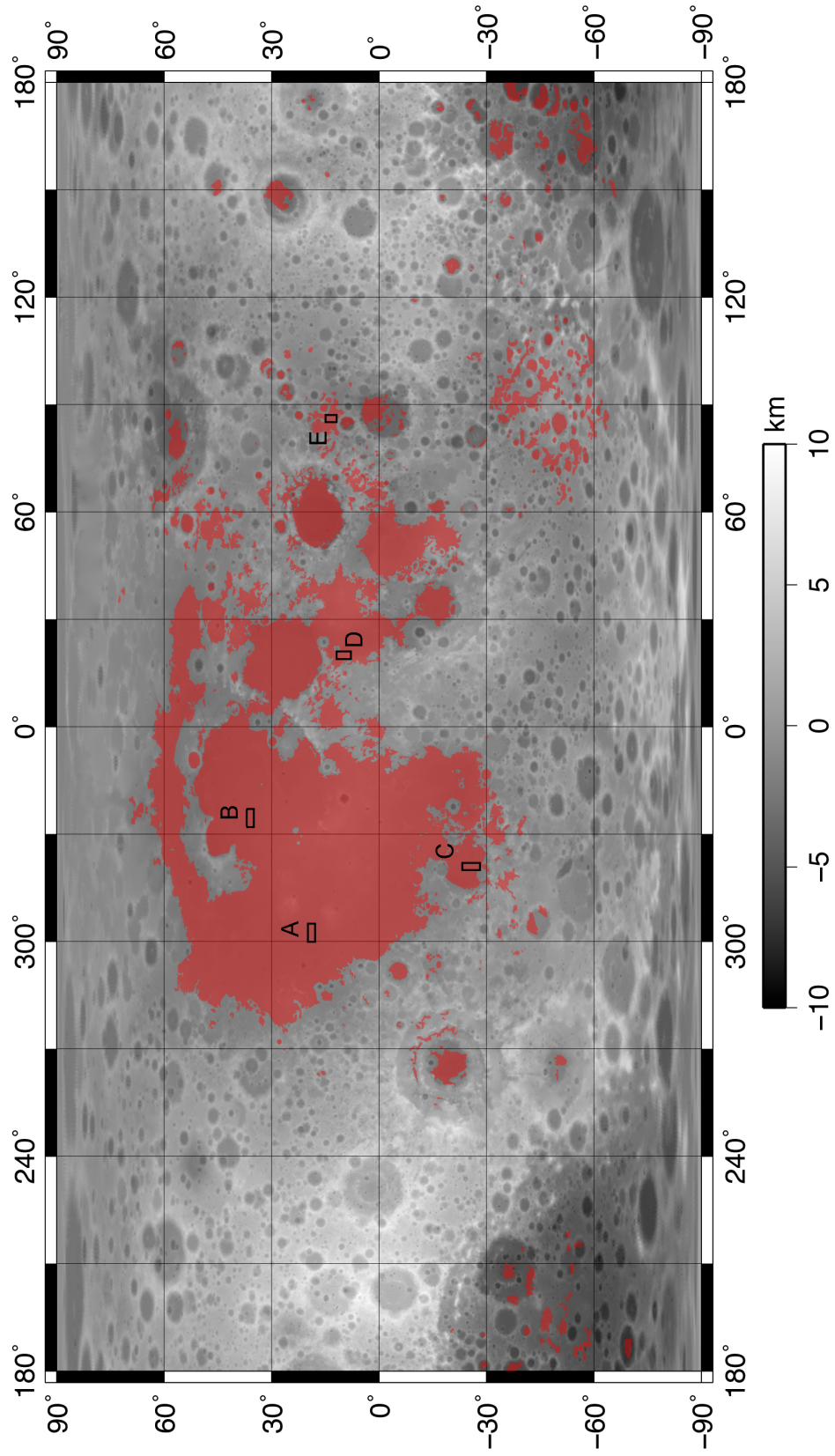


Figure 3.8: Context map for sampled regions within the lunar maria, showing the outline of mare deposits (Wilhelms et al., 1971, 1977; Scott and McCauley, 1977; Lucchitta and Center, 1978; Stuart-Alexander and Center, 1978; Wilhelms et al., 1979) overlain on the lunar topography in a simple cylindrical projection.

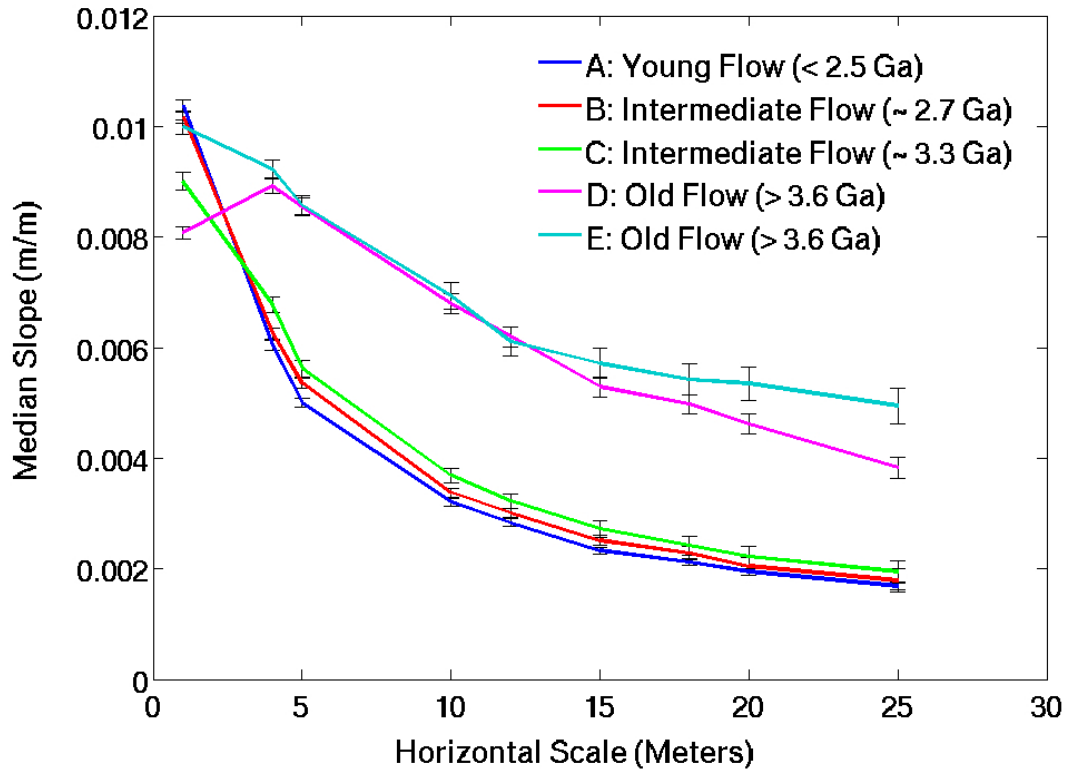


Figure 3.9: Comparison of differential slopes at many baselines within the sampled regions of the lunar maria. Standard 2σ error bars represent the spread of the distribution of median differential slopes within each sampled region and for each baseline considered.

(Hiesinger *et al.*, 2010). Letters in the legend correspond to the boxes in the context map (Fig. 3.8).

The youngest mare units, within Oceanus Procellarum and Mare Imbrium, are rough only at the smallest scales, while successively older flows (e.g., those within Mare Tranquilitatis and Mare Marginis) contain significant roughness components at longer baselines. At the smallest scale, median differential slope remains roughly constant among all sampled regions, suggesting that perhaps crater saturation at small ($D < 100$ m) scales occurs relatively swiftly. This observation is consistent with Kreslavsky *et al.* (2013) and Rosenburg *et al.* (2011), who note that at hectometer scales, roughness is approximately constant on global scales, both on maria and highlands terrain. Differential slopes at larger baselines vary systematically with the age of the surface considered, although, as Kreslavsky *et al.* (2013) point out, the roughness of mare surfaces is not a function of age alone, and specific regions of young terrain can be found that are rougher than older mare surfaces.

3.4 Summary

Roughness maps provide a means of analyzing large-scale variations in typical surface texture at a range of finer scales. As such, they are useful tools for geologic mapping and interpretation, with specific application to the identification of geologic units, assessment of relative ages, and characterization of the effects of competing surface processes acting at different scales. Detailed studies of local regions, like those discussed above for the lunar south pole, Shackleton crater, and mare surfaces of varying age, extend and focus the analysis initiated in the global roughness maps of *Rosenburg et al.* (2011) (Chapter 2) and *Kreslavsky et al.* (2013).

Focusing on the lunar south pole, where the confluence of LOLA tracks results in a high density of elevation measurements conducive to detailed study using differential slopes, we find that many features express unique roughness signatures, including rough, Copernican-age craters and their associated ray systems. Aside from a slight enhancement at the ~ 560 -m scale, South Pole-Aitken basin, the largest and oldest basin on the Moon, is poorly defined in the differential slope map shown in Figure 3.1, despite its obvious expression in the topography (*Garrick-Bethell and Zuber*, 2009). Complex craters and basins ranging from $D \sim 50$ to ~ 300 km exhibit a typical sequence of approximately concentric roughness zones: a bright white (rough at every scale) ring corresponding to the rim crest, a dark blue (smooth at all scales) annulus corresponding to the steep inner walls, and discontinuous arcs that appear red (rough at the ~ 560 -m scale) in the composite color maps (Fig. 3.1), which correspond to hummocky, slumped material from the crater walls, segments of the peak-crater ring, and the central peak formations. Where the interiors of large basins have been filled and reworked by volcanic flows, as in Antoniadi and Schrödinger, the topography is smoother than the rest of the crater floor, rough only at the smallest scale considered, ~ 57 m. Small craters ($D < 50$ km) also exhibit many of these key features, notably the rough rim crest and steep inner walls. The consistency of these roughness units across crater diameters reflects the underlying consistency in the scale of crater modification processes such as mass wasting and impact gardening.

Shackleton crater, of interest for its unique illumination conditions, possesses several distinct

roughness units that correlate well with geologic units mapped using the elevation data. Brightness measurements at the 1064-nm scale of the LOLA laser are consistent with the downslope movement of material on the steep crater walls, exposing fresher, brighter material underneath, while the relatively bright crater floor can be explained either by decreased space weathering in the shadowed crater interior or a thin surface layer of material containing a significant fraction of water ice (*Zuber et al.*, 2012a). The dark blue appearance of the crater walls and the red hue of the mound unit (interpreted as a potential slump deposit) in Figure 3.6 supports the mass wasting hypothesis suggested by the brightness measurements. Regions of suspected secondary craters also are shown to have a distinct roughness signature in the differential slope map at these baselines, demonstrating the utility of roughness measures in distinguishing between primary and secondary craters.

Finally, the evolution of roughness on mare surfaces of varying age is examined using differential slopes at several different baselines within several mare units whose ages have been determined via crater counts by *Hiesinger et al.* (2010). We find that roughness at the shortest scale accessible with LOLA, ~ 57 m, is approximately constant across all sampled regions, suggesting that crater saturation at small scales ($D < 100$ m) has occurred. At larger scales, older mare units are rougher than their younger counterparts, having had more time to collect craters within a broader range of diameters.